Driving Forces underlying Selectivity Filter Gating in the MthK Potassium Channel

Wojciech Kopec[1*], Andrew S. Thomson[2], Bert L. de Groot[1], Brad S. Rothberg[2]

[1]Computational Biomolecular Dynamics Group, Max Planck Institute for Multidisciplinary Sciences, Am Fassberg 11, 37077 Göttingen, Germany

[2]Department of Medical Genetics and Molecular Biochemistry, Temple University Lewis Katz School of Medicine, Philadelphia, PA 19140, USA

*corresponding author

ABSTRACT

K^+ channel activity can be limited by C-type inactivation, which is likely initiated in part by dissociation of K^+ ions from the selectivity filter, and modulated by side chains surrounding the selectivity filter. Whereas crystallographic and computational studies have linked inactivation to a "collapsed" selectivity filter conformation in the KcsA channel, the structural basis for selectivity filter gating in other K^+ channels has been less clear. Here, we combined electrophysiological recordings with molecular dynamics based, *in silico* electrophysiology simulations to study selectivity filter gating in the model potassium channel MthK and the MthK mutant V55E (analogous to KcsA E71) in the pore-helix. We find that MthK V55E has lower open probability than the WT channel, due to decreased stability of the open state. Simulations account for aspects of these observations on the atomistic scale, showing that ion permeation in V55E is differentially altered in two distinct orientations of the E55 side chain. In the 'vertical' orientation of E55, in which E55 forms a hydrogen bond with D64 (as observed with KcsA WT channels), the filter displays reduced conductance compared to MthK WT. In contrast, with 'horizontal' orientation, K^+ conductance is similar to MthK WT; however the filter is less stable in the conductive conformation. Surprisingly, transitions of MthK WT and V55E channels to the non-conducting (inactivated) state observed in simulations are associated with a widening selectivity filter, unlike the narrowing selectivity filter observed with KcsA, and similar to recent structures of stably-inactivated *Shaker* W434F and Kv1.2 W362F mutants.

INTRODUCTION

Potassium (K^+) channels are critically important in the control of many cellular functions, including action potential firing, neurotransmitter and hormone release, and muscle contraction [1]. A great deal of effort has been focused on understanding the molecular basis of K^+ permeation and channel gating, and it is now clear that K^+ channels gate at multiple structural loci [2]. For example, in voltage-gated K^+ channels as well as inwardly-rectifying K^+ channels, the pore-lining helices from each subunit can form a constriction (activation gate) at the cytosolic entrance to the pore (S6 gating) [3–5], whereas these and other K^+ channels can also undergo conformational changes near the selectivity filter, at the extracellular end of the pore (SF gating), to gate ion permeation (**Fig. 1 A, B**) [6,7]. A combination of structural and functional studies has revealed that the mechanisms underlying each of these gating processes are unlikely to arise from a single blueprint, and that diversity among K^+ channels is likely to have yielded several complementary mechanisms to underlie gating that may be coupled to transmembrane voltage, ligands, or other stimuli [8–11].

It was observed previously that the prokaryotic K^+ channel MthK exhibits SF gating that shares many properties in common with C-type inactivation of Kv channels. Specifically, channel opening is greatly decreased by increasing depolarization and decreasing extracellular potassium concentration ($[K^+]$), and the gating process shows a selective sensitivity to cationic channel

blockers, similar to that observed with the modulatory effect of quaternary ammonium derivatives on C-type inactivation in the *Shaker* K^+ channel [9,12–16]. Interestingly, the pore-helix glutamate that is a key determinant of inactivation in KcsA (E71) does not play a role in MthK gating; instead, this position contains a hydrophobic valine sidechain (V55, **Fig 1. C, D**), which is the same residue found at this position in *Shaker* (V438), as well as mammalian Kv1.2 (V366) channels. This implies that the molecular driving forces and structural changes underlying SF gating among these channels may be different from one another.

To better understand the molecular basis for SF gating, we examined the functional consequences of substituting V55 in MthK with (protonated) glutamate (**Fig 1. E**) by electrophysiology, and analyzed potential underlying mechanisms by *in silico* electrophysiology molecular simulation. We observe that the V55E mutation yields a gating phenotype with markedly reduced open state stability, manifested as decreased channel open probability and decreased open times over a wide range of voltages. On the molecular level, simulations reveal two distinct orientations of the E55 side chain ('vertical' and 'horizontal') that differentially affect SF properties. The 'vertical' orientation is reminiscent of E71 seen in structures of KcsA (**Fig 1. D**), where it hydrogen bonds with an aspartate behind the SF (D80 in KcsA; D64 in MthK). In this orientation, the K^+ conductance of MthK V55E is low. In the second, 'horizontal' orientation, that is with the E55 side chain oriented perpendicular to the membrane, K^+ conductance is similar to MthK WT, but longer simulations show that it has an increased propensity to enter the non-conductive state. Further, in our simulations SFs of both WT and V55E channels undergo gating transitions that are structurally similar to C-type inactivated conformations observed in stably-inactivated mutants of *Shaker* and Kv1.2 channels. In a full accord with electrophysiology, V55E SF shows in simulations a larger degree of instability than WT, which arises from the compromised hydrogen bond network and water penetration behind the SF when the E55 side chain adopts the 'horizontal' orientation. Together, these data suggest a mechanism for SF gating (inactivation) in MthK channels, and highlight the critical role for interactions between the SF and pore-helix in stabilizing the K^+ ion conduction pathway.

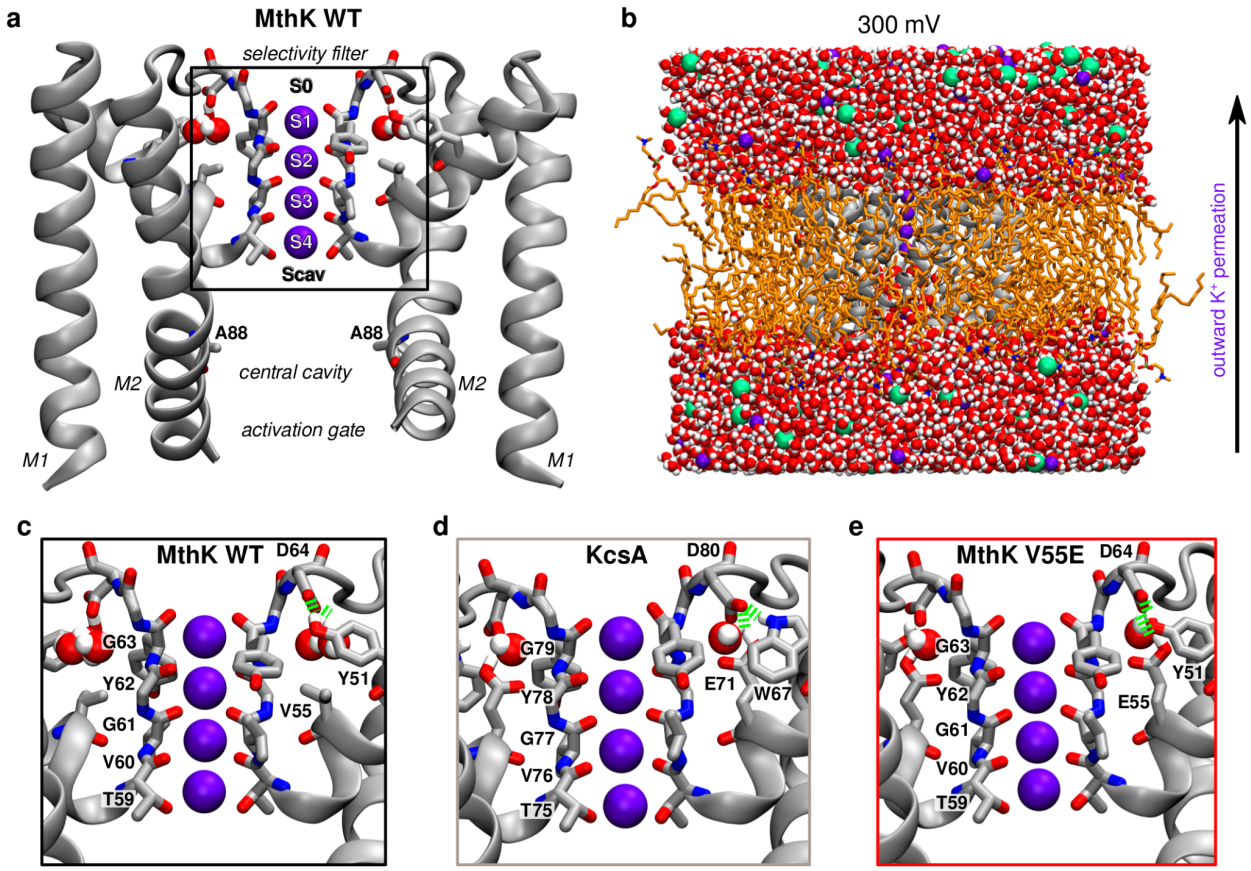

Figure 1 Basic architecture of a potassium channel. A, Crystal structure of MthK in an open state (PDB ID: 3LDC, only two diagonally opposite subunits of a tetramer are shown), with highlighted important elements - the selectivity filter in its conductive conformation consists of 4 main potassium binding sites S1-S4 and additional binding sites S0 and Scav. The central cavity, normally filled with water molecules, is located below the filter and above the activation gate. B, A snapshot of an all-atom system used in MD simulations. The channel is shown in grey, lipids (POPC) in orange, water as red-white spheres, potassium ions as purple spheres and chloride ions as green spheres. Transmembrane voltage of 300 mV was used in simulations, resulting in an outward permeation of potassium ions through the channel as indicated by the arrow. C-E, Closer view on an interaction network behind the selectivity filter. In wildtype MthK, D64 makes hydrogen bonds (green springs) with Y51 and two crystallographic water molecules (C). In KcsA (PDB ID: 1K4C, D) a residue corresponding to Y51 is W67. Additionally a protonated glutamate (E71, V55 in MthK) takes part in the same interaction network, with only one water molecule. The model of MthK V55E (E) is based on MthK WT, with V55 replaced with protonated E71 from KcsA and one water molecule.

RESULTS

Electrophysiology

Mutation of E71 to alanine, in the pore-helix of KcsA, was observed to abrogate a key interaction with the carboxylate and D80, resulting in stabilization of the open state and loss of inactivation in KcsA channels. It was observed previously that MthK channels can also exhibit

an inactivation-like phenomenon, in which the open state is stabilized by occupancy of a K^+-selective site at the external end of the SF [9,12].

To determine whether MthK inactivation and KcsA inactivation might arise through similar molecular interactions, we first examined functional consequences of substituting MthK V55 (at the position analogous to KcsA E71) with glutamate. We observe that with symmetrical 200 mM K^+ solutions, MthK WT channels, activated by 100 μM Cd^{2+} at the cytosolic side of the channel, gate with high open probability (Popen) of >0.9 at voltage ranging from -180 to +140 mV (**Fig. 2**) [12,17,18]. At strongly depolarized voltages (>140 mV), Popen decreases sharply with increasing depolarization, with a voltage-dependence of e-fold per 14 mV and a $V_{1/2}$ for this decrease at 190 ± 1.5 mV (7). This robust decrease in Popen is enhanced by decreasing external [K^+] (K^+_{ext}), such that a decrease from 200 mM to 5 mM K^+_{ext} shifts the $V_{1/2}$ from 190 to 95 ± 2.6 mV (**Fig. 2 C**) [12]. These gating effects are described by a model in which voltage-dependent outward K^+ ion movement, followed by dissociation of a K^+ ion from the external end of the SF, leads to a conformational change within the SF that consists of an off-axis rotation of a carbonyl group (at V60) that normally lines the selectivity filter [9,12]. This carbonyl rotation can halt conduction and thus gate the channel [12,19].

In contrast, with symmetrical 200 mM K^+ solutions, the MthK V55E mutant reaches a maximum Popen of 0.71 ± 0.01 at -125 mV, and Popen decreases with either depolarization or stronger hyperpolarization (**Fig. 2 C**). Over the entire 400-mV voltage range examined in these experiments (from 200 to +200 mV), MthK V55E channels exhibited lower Popen than MthK WT channels recorded under the same conditions.

The single-channel currents in **Fig. 2 A** suggested that the basis for the decreased Popen in MthK V55E channels may be a decrease in mean open time compared to WT. Consistent with this observation, **Fig. 2 D** illustrates that the mean open time of V55E channels is briefer than WT over voltages ranging from -200 to +200 mV. At voltages more depolarized than -75 mV, mean open times of V55E channels were decreased by 10- to 100-fold compared to WT. In contrast, closed times of V55E channels were increased generally by less than two-fold over the range of 150 to +150 mV (**Fig. 2 E**). In addition, mean open time and Popen in V55E channels exhibit the same weak voltage-dependence over a very wide voltage range, with maximal mean open time of 6.7 ± 0.2 ms at -125 mV. Mechanistically, this indicates that the V55E mutation leads to decreased lifetime, and thus decreased energetic stability of the open (conducting) state.

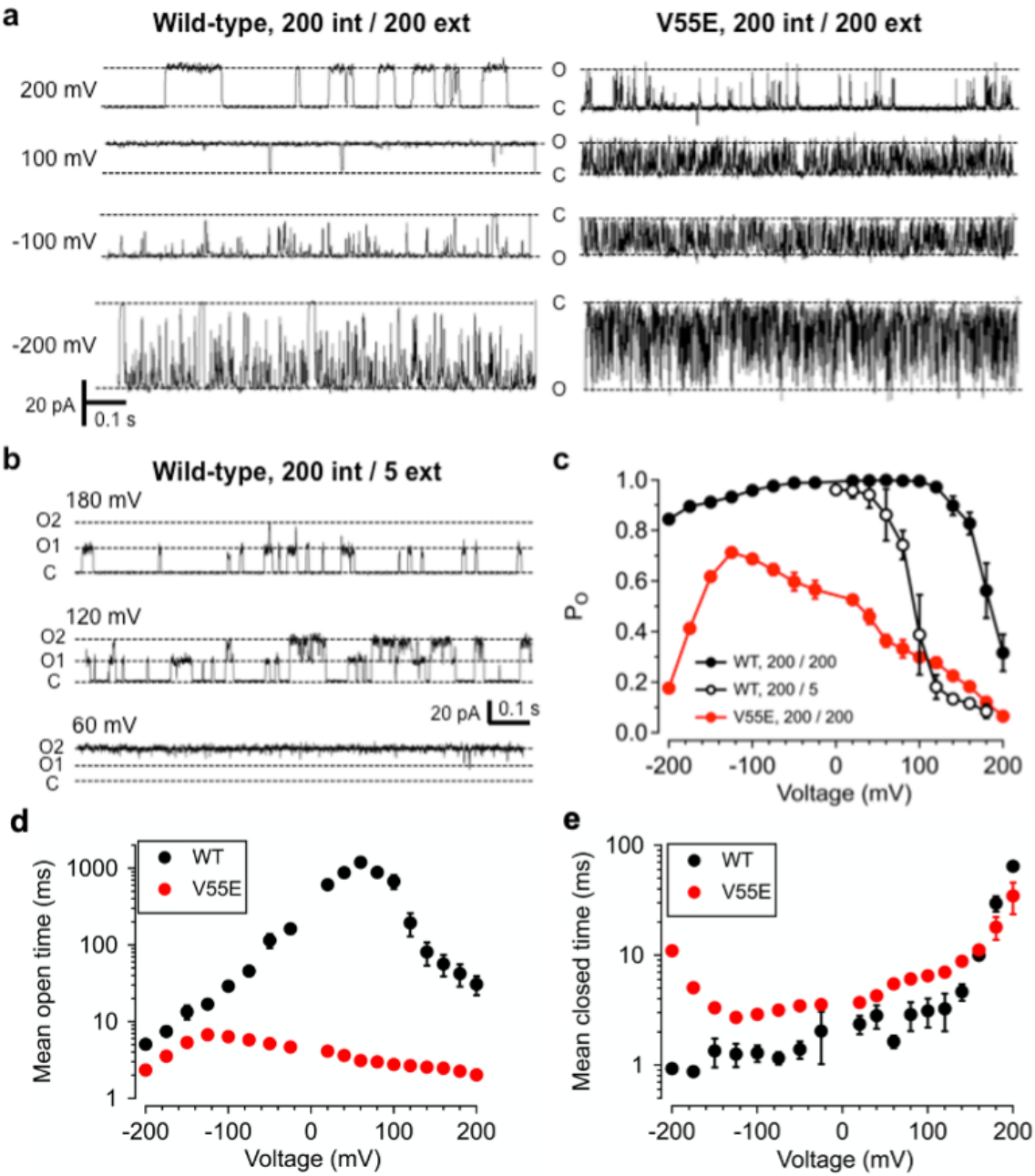

Figure 2 Effects of V55E mutation on MthK channel gating. A, Representative single-channel current through MthK wid-type and V55E channels over a range of voltages. For these recordings, solutions at both sides of the membrane contained 200 mM KCl. "O" and "C" indicate open and closed channel current levels, respectively. Strong depolarization (200 mV) leads to decreased open probability (Po) for wild-type channels, and V55E channels consistently display briefer openings than wild-type at all tested voltages. B, current through MthK wild-type channels with 5 mM external K^+. This bilayer contained two active channels, indicated by open levels "O1" and "O2". Lower external [K^+] enhances inactivation at mildly depolarized voltages. C, Po vs. voltage for wild-type (WT) channels with 200 mM (black circles, n=5 bilayers) or 5 mM external K^+ (open circles, n=3 bilayers), compared with V55E with 200 mM external K^+ (n=5 bilayers). D, MthK WT channel open times were voltage dependent, with a maximal mean open time of 1200 +/- 120 ms at 60 mV; in contrast V55E were much briefer, with the mean open

time not exceeding 6.7 +/- 0.2 ms over a 400 mV range. E, WT and V55E closed times were similar over a wide range of voltages, consistent with the idea that the major effect of the V55E mutation was to destabilize the open/conducting state relative to WT. $[K^+]_{ext}$ = 200 mM (WT n=5; V55E n=5).

Shorter in silico electrophysiology simulations - Amber force field

To probe the effects of the V55E mutation on the atomistic scale, we used our previous computational protocol to monitor changes in outward current in MthK caused by opening and closing of the inner helices (the activation gate, **Fig. 3 A**) [20]. When compared to the WT channel, currents in V55E display a similar overall behavior, with an initial increase in magnitude upon the activation gate opening, followed by a decrease at larger openings (**Fig. 3 B**). In WT, we have previously traced down this behavior to the variations in the width of the S4 binding site, formed exclusively by T59 (**Fig. 3 A)**. Indeed, when T59 CA-CA distance (i.e. S4 width) is used as an opening coordinate, currents in V55E show a similar trend upon S4 opening as in WT (**Fig. 3 C**). In contrast however, the maximum current in V55E (~9 pA) is markedly lower than the WT maximum current (~16 pA), suggesting that an additional energetic barrier for ion permeation (apart from the one imposed by T59) exists somewhere along the permeation pathway.

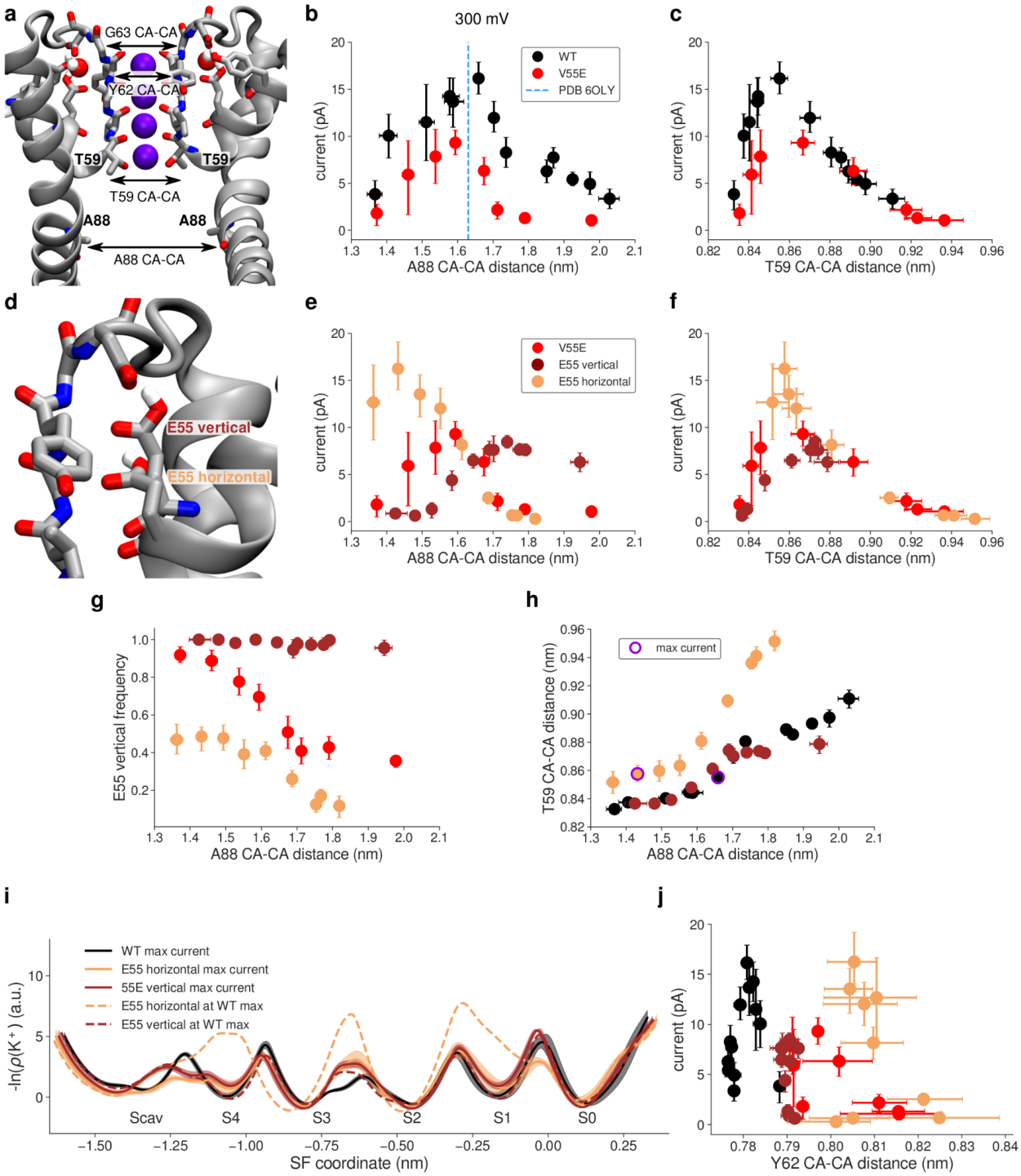

Figure 3 Current regulation in MthK V55E in MD simulations with the AMBER force field. A, Starting structure of MthK V55E and the definitions of distances used as opening coordinates (A88 CA-CA distance: activation gate; T59 CA-CA distance: S4 width). B, Outward current through MthK WT (black traces) and MthK V55E (red traces) as a function of the activation gate opening. Blue vertical line marks the largest opening level seen experimentally. C, Same as B, but with the S4 width used as the opening coordinate. D, Two rotameric states (orientations) of E55 observed in MD simulations. E, Outward current in 'E55 vertical' (brown traces) and 'E55 horizontal' (light orange traces) simulation sets

in comparison to current in V55E (red traces), as a function of the activation gate opening. F, Same as E, but with the S4 width used as the opening coordinate. G, Frequency of the 'vertical' rotameric state of E55 as a function of the activation gate opening. H, Correlation between S4 width and the activation gate opening in 'E55 vertical' and 'E55 horizontal' in comparison to WT. Points for which the maximal current of ~16 pA was recorded are indicated by a violet ring. I, Negative logarithmic densities ('free energy profiles') of K^+ ions in the SF. Minima correspond to stable ion binding sites and maxima to free energy barriers between them. J, Currents in all systems with the Y62 (forming S1 and S0 sites) CA-CA distance used as an opening coordinate. On all panels, error bars represent 95% confidence intervals.

In simulations of MthK V55E, we observed that the E55 side chain adopts two distinct rotameric states (**Fig. 3 D**) - one that is seen in crystal structures of KcsA, where the (protonated) side chain of E55 (E71 in KcsA) hydrogen bonds with the side chain D64 (D80 in KcsA) behind the SF ('vertical' orientation). In the second orientation, this hydrogen bond is broken, and instead the sidechain of E55 adopts a more in-plane orientation with respect to the membrane ('horizontal' orientation). We suspected that this rotameric transition might have a large influence on the conductive properties of the SF. For a clearer picture, we performed separate simulations with the E55 side chain restrained to one of the two orientations (simulation sets 'E55 vertical' and 'E55 horizontal'). These simulations show that the orientation of the E55 side chain has a major effect on current, and on its dependence on both gate and S4 opening (**Fig. 3 E, F**).

When the E55 side chain adopts the 'vertical' orientation, the currents are markedly lower than in the non-restrained case, at low and moderate activation gate openings, and only at larger openings reach the level of 7-8 pA (**Fig. 3 E**, brown traces). Furthermore, the current does not decrease again at very large openings. The reason for that is clear when the S4 width is used as the opening coordinate (**Fig 3 F**, brown traces) - in 'E55 vertical' the S4 does not get wider than ca. 0.88 nm, showing that the activation gate S4 coupling is restricted when the E55 side chain adopts the 'vertical' orientation, in contrast to non-restrained simulations of V55E (and WT, see **Fig. 3 C**).

However, when the E55 side chain adopts the 'horizontal' orientation, the current reaches its maximum value at small activation gate openings of ~1.43 nm (**Fig. 3 E**, light orange traces), in contrast to 1.6-1.65 in the non-restrained case (and WT). Interestingly, the S4 width in 'E55 horizontal' in this case is identical to MthK WT, when it reaches its maximum current. In other words, the 'horizontal' orientation of the E55 side chain affects the activation gate - S4 coupling: the S4 binding site is able to open more at smaller activation gate openings. Importantly, the maximum current in 'E55 horizontal' reaches the value of MthK WT, showing that MthK WT and V55E can conduct ions at the same rate, in a good agreement with experiments (**Fig 2 A, B**).

Overall, currents in non-restrained MthK V55E (**Fig. 3 E,** red traces), are affected not only by the activation gate opening (as in WT), but additionally also by the rotameric state of the E55 side chain. The preference for 'vertical' vs.' horizontal orientation' of E55 depends on the gate opening too (**Fig. 3 G**, red traces).

Having discovered the intertwined effects of activation gate opening, S4 width and the E55 side chain orientations on ion permeation, we wondered where the additional energetic barrier, best

seen in both non-restrained V55E and 'E55 vertical' simulations (**Fig. 3 E**), is located. More precisely, why these simulations do not show currents as high as MthK WT or 'E55 horizontal', even though in all these cases the optimal width of S4 (~0.86 nm, **Fig. 3 F, H**) is reached. To gain additional insights, we calculated negative logarithms of potassium densities in the SF (**Fig. 3 I**) that might be treated as approximate, one dimensional free energy profiles for ion permeation. A comparison with the profile for MthK WT (black curve) reveals that in MthK V55E (solid brown and light orange curves) the barriers are reduced at the entry to the SF (between Scav and S4, as well as between S4 and S3), for both orientations of the E55 side chain. In turn, however, there is a larger barrier for 'E55 vertical', located between S1 and S0 (both brown curves). This is the highest energetical barrier, suggesting that it is the rate-limiting barrier. Consequently, the width of the SF between S1 and S0 (measured as the CA-CA distance of Y62, **Fig. 3 J**) does not show any variation in 'E55 vertical' being effectively locked at ~0.79 nm, in stark contrast to both MthK WT and 'E55 horizontal'. Interestingly, this value lies between those observed in MthK WT and 'E55 horizontal' suggesting that this particular value leads to a very strong binding of a K^+ ions to S2. Indeed in 'E55 vertical' the occupancy of S2 by K^+ ions is >0.95, compared to ~0.82 in WT

In 'V55E horizontal', at an opening that shows the maximum current, the free energy profile is quite flat with low barriers, consistent with the observed high current (**Fig. 3 I**, light orange curve). The profile at a larger opening (dashed curve) reveals the effect of the 'horizontal' orientation of E55 on S4 in the AMBER force field - the S4 binding site is compromised (a free energy minimum is replaced by a maximum), which likely gives rises to other very high barriers, drastically decreasing the current at larger openings in 'E55 horizontal'.

Shorter in silico electrophysiology - CHARMM force field

Subsequently, we simulated the same systems in the CHARMM force field, to see whether the previous observations are force field dependent. In our previous study of MthK WT, both force fields showed the same trend in the current dependence on the lower gate opening, as well as very similar maximum currents [20].

Overall, simulations of V55E done with the CHARMM force field show little currents (up to 1.5 pA, i.e. more than an order of magnitude smaller than in WT) at all levels of the lower gate opening (**Fig. 4 A**). The S4 does however become wider in V55E, similarly to WT (**Fig. 4 B**), suggesting that a large free energy barrier for ion permeation exists somewhere else in the SF. In contrast to AMBER simulations, where we observed two rotamers of the E55 side chain, in CHARMM the E55 side chain adopts almost exclusively the 'vertical' orientation (**Fig. 4 C,** red traces). Initial tries of inducing the 'horizontal' orientations were unsuccessful; we then used some of the 'horizontal' orientations seen in AMBER for further simulations with the CHARMM force field, imposing strong position restraints (**Fig. 4 C**, light orange traces). For completeness, we also simulated a system with distance restraints present in the 'vertical' orientation (**Fig. 4 C**, brown traces). This simulation set, 'E55 vertical', behaves almost identical as the unrestrained case, indicating that the application of restraints has negligible effects on the

overall channel function.

Similarly to AMBER simulations, when the E55 side chain adopts the 'horizontal' orientation in CHARMM, the channel is able to permeate K^+ ions as efficiently as WT (**Fig. 4 D**). In CHARMM however, that happens at the same gate opening level as in WT, which somewhat unexpectedly corresponds to slightly larger openings of the S4 in 'E55 horizontal' (**Fig. 4 E, F**). These observations suggest that the free energy barrier imposed by T59 is not always the dominating one in CHARMM. Indeed, in the WT channel, there is a barrier of a similar height located between S2 and S1 binding sites (**Fig. 4 G**, black traces). This barrier becomes dominant in 'E55 horizontal', even though the barrier between S4 and S3 got lowered further, explaining the same maximal current in both WT and 'E55 horizontal' simulations.

The remaining question is, again, why in unrestrained V55E and 'E55 vertical' simulations ion conduction is so low (max. 1.5 pA in CHARMM). The free energy profiles (**Fig. 4 G**, brown traces) show several very high barriers, as well as severely affected Scav and S0 ion binding sites. The lack of the Scav binding site can be explained by a constant occupation of S4 by an ion in the case of non-permeating ion, which would then electrostatically repel other ions approaching Scav, which is structurally not well defined (**Fig. 1 A**). However, the lack of the S0 binding site is more puzzling, also because it was preserved in AMBER simulations. The analysis of CA-CA distances of S0-forming G63 (**Fig. 4 H**) reveals that the 'vertical' orientation of the E55 side chain makes S0 too narrow, and in consequence it likely cannot bind K^+ ions anymore. Only upon the E55 side chain rotation toward the 'horizontal' orientation, S0 becomes as wide as in MthK WT, which correlates with the increased current (**Fig. 4 H**, black and light orange traces).

Summarizing, CHARMM and AMBER show marked differences in the exact behavior of the MthK V55E SF, however they are in a broad accord in at least three main points: i) ion permeation in MthK V55E depends not only on the coupling between the activation gate and S4, but also on the rotameric state of the E55 side chain, ii) the 'vertical' E55 orientation, i.e. hydrogen-bonded with both D64 and Y51 (**Fig. 1 E**), reduces currents by imposing additional free energy barriers for ion permeation in the SF, iii) the 'horizontal' orientation of E55 increases currents in V55E to WT-like levels, by reducing these free energy barriers, especially in the upper part of the SF.

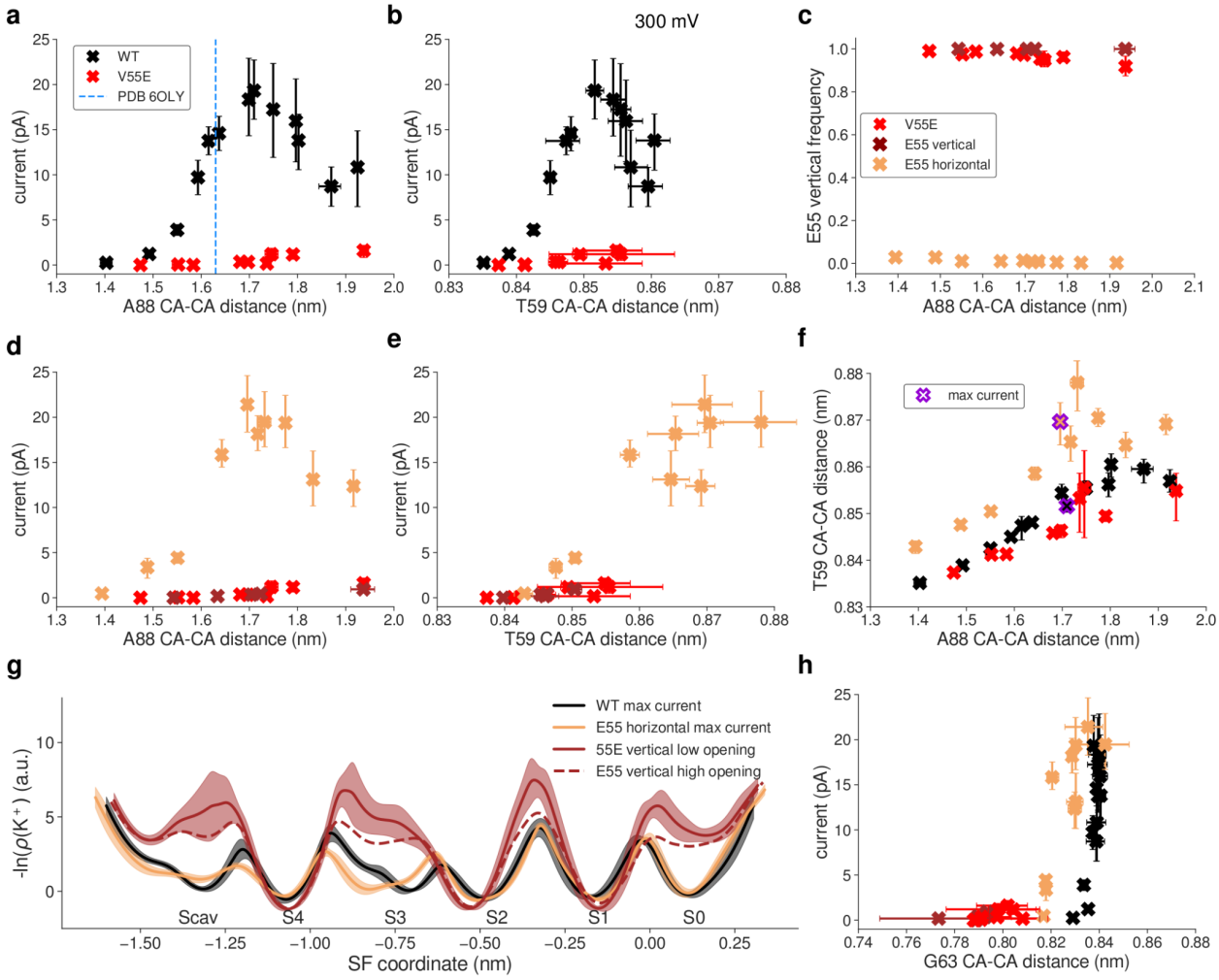

Figure 4 Current regulation in MthK V55E in MD simulations with the CHARMM force field. A, Outward current through MthK WT (black traces) and MthK V55E (red traces) as a function of the activation gate opening. Blue vertical line marks the largest opening level seen experimentally. B, Same as A, but with the S4 width used as the opening coordinate. C, Frequency of the 'vertical' rotameric state of E55 as a function of the activation gate opening. D, Outward current in 'E55 vertical' (brown traces) and 'E55 horizontal' (light orange traces) in comparison to current V55E (red traces), as a function of the activation gate opening. E, Same as D, but with the S4 width used as the opening coordinate. F, Correlation between S4 width and the activation gate opening in 'E55 vertical' and 'E55 horizontal' in comparison to WT. Points for which the maximal current of ~20 pA was recorded are indicated by a violet cross. G, Negative logarithmic densities ('free energy profiles') of K ions in the SF. Minima correspond to stable ion binding sites and maxima to free energy barriers between them. H, Current in all systems with the G63 (forming S0 site) CA-CA distance used as an opening coordinate. On all panels, error bars represent 95% confidence intervals.

Longer in silico electrophysiology simulations

Apart from faster motions occurring on the tens and hundreds of nanoseconds timescale studied above, we were also interested if we can directly probe SF gating (inactivation), i.e. conformational transitions of the SF, in MD simulations. Even though in reality, the timescales of

such transitions are at least in the millisecond range [21], way above the standard MD range, they have nevertheless been observed in simulations in a few cases [22,23]. Structures of KcsA and stably-inactivated mutants of voltage-gated K^+ channels (*Shaker* W434F and Kv1.2 W362F) revealed that C-type inactivation-related conformational changes at the SF can follow at least two distinct paths (**Fig. 5**) [24–26]: in KcsA the SF pinches (constricts) at the level of the 'first' glycine (G77, G61 in MthK), whereas in voltage-gated channels the SF dilates (widens) at the level of the 'second' glycine (G446 in *Shaker,* G374 in Kv1.2, G63 in MthK). In the latter case, this SF dilation is accompanied by a breakage of hydrogen bonds between aspartate (D447 in *Shaker*, D375 in Kv1.2, D64 in MthK) and tyrosine/tryptophan (W434 in *Shaker*, W362 in Kv1.2, Y51 in MthK) (replaced by phenylalanine in stably-inactivated mutants) residues, and flipping of aspartate side chains toward the extracellular side. In contrast, these hydrogen bonds are retained during SF inactivation in KcsA and aspartate (D80) flipping has not been observed (**Fig. 5 B**). Previous works on KcsA revealed that the SF pinching occurs in MD simulations on the microsecond timescale with the CHARMM force field, and the SF adopts the crystal structure-like conformation (PDB ID: 1K4D) [22]. Our previous work on the Kv1.2 channel predicted aspartate flipping and SF dilation using the same force field [27] (**Fig. 4 C**), before recent cryoEM structures of stably-inactivated *Shaker* W434F and Kv1.2 W362F channels [24,26].

Here, we probed the stability of the SF of both MthK WT and the V55E in 20 independent, 5 us long MD simulations per force field/system (400 us in total), under applied voltage (300 mV), and at a large activation gate opening, which speeds up SF conformational transitions [22,23]. We focused on whether the interactions between D64 and Y51 are retained or broken (**Supplementary Fig. 1-4**, the distance larger than ca. 0.7 nm indicates a broken interaction and a subsequent aspartate flip), and on the changes in the SF geometry, at the level of both 'first' and 'second' glycines (G61 and G63, **Supplementary Fig. 5-8** and **Supplementary Fig. 9-12**, respectively).

In many of our simulations, the SF of MthK V55E undergoes dilation/constriction transitions at the level of G63 (and also G61), which is preceded by at least one broken D64-Y51 interaction (aspartate flip) (**Supplementary Fig. 2, 4**), in both force fields, whereas in MthK WT such transitions occur only in the CHARMM force field (**Supplementary Fig. 1, 3**). Specifically, as the aspartate flip is common in our simulations, and has been previously connected to SF widening at G63 in Kv channels, we used G63 CA distance variations as a coordinate defining conductive and inactivated filter conformations (**Supplementary Fig. 9-12**). Based on this coordinate, we counted the conductive to non-conductive (inactivated) transitions occurring in independent simulations (**Fig. 5 G, H**). On the MD simulations timescale used here, these transitions occur irreversibly, i.e. maximally once per simulation. In the AMBER force field, we observed 7/20 such 'inactivation transitions' for V55E, whereas it did not occur at all for WT. In the CHARMM force field, V55E transitioned to the inactivated state in 19/20 simulations, whereas only 7/20 'inactivation transitions' were observed for WT. Thus, these simulations clearly show that MthK V55E has an increased propensity to enter the inactivated conformation

as compared to WT. V55E thus reduces the stability of the conductive conformation of the SF and promotes the inactivated conformation, which structurally resembles the SF conformations of stably-inactivated mutants of *Shaker* and Kv1.2 channels (**Fig. 5 D-F**). Further, this computationally predicted lower stability of the conductive conformation in V55E is in excellent agreement with electrophysiological measurements (**Fig. 2 C**).

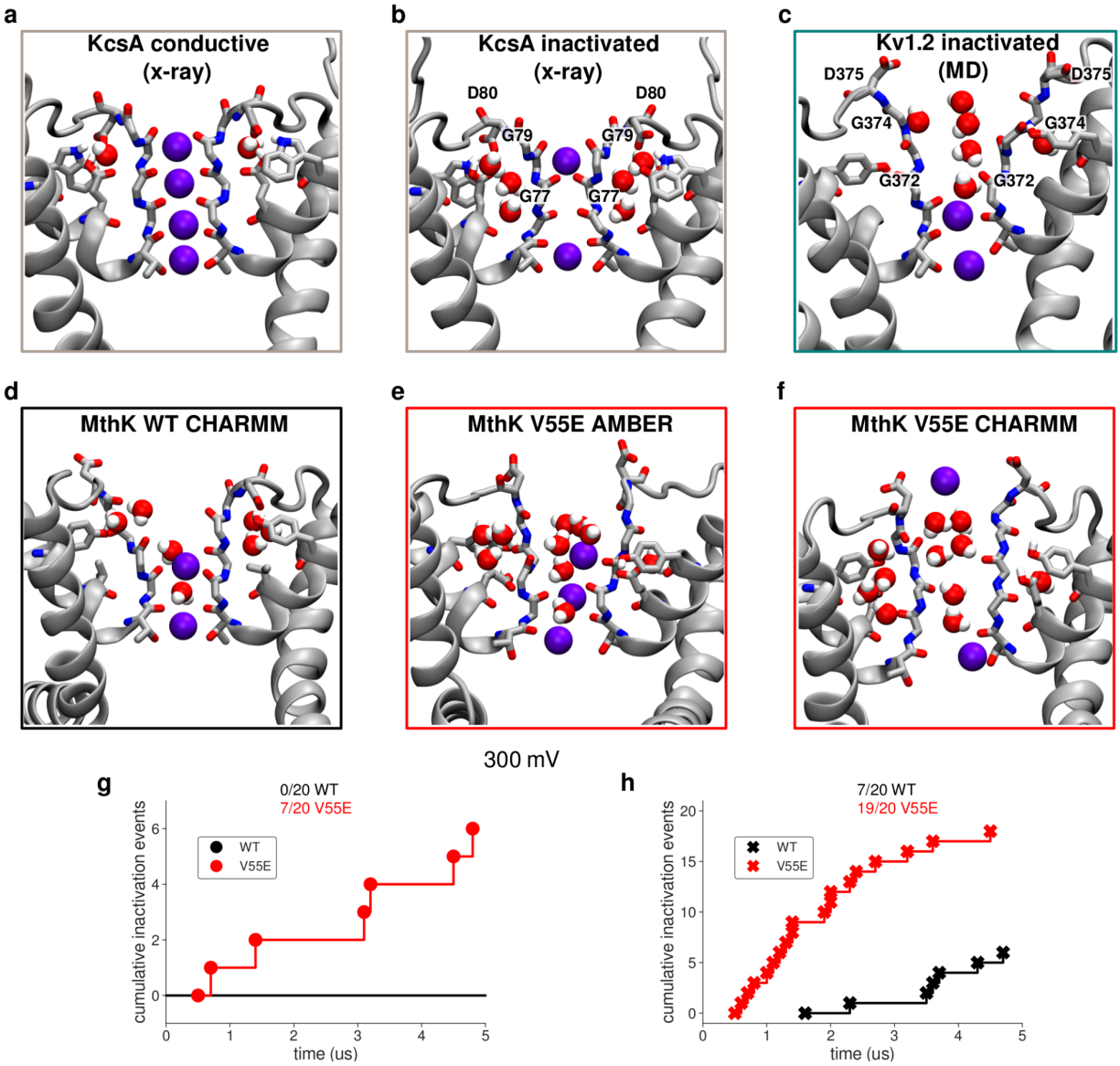

Figure 5 Conformations of inactivated filters in different K^+ channels. A, Typical conductive SF conformation shown for reference (PDB ID: 1K4C). B, Inactivated ('constricted' or 'pinched') KcsA filter (PDB ID: 1K4D). The filter narrows at the level of the 'first' glycines (G77) C, Snapshot from previous MD simulations of the Kv1.2 W362Y channel, that shows a loss of a hydrogen bond between D375 and Y362, and flipping of D375 sidechain, accompanied by the SF widening/dilation, at the level of the 'second' glycines (G374). D-F, Examples of SF conformations observed in this work in long simulations of either MthK WT (D) or MthK V55E (E, F). In all cases, flipping of aspartates (D64) is observed, as well as widening at the level of the 'second' glycines (G63). G, H, Cumulative inactivation

events recorded in simulations with AMBER (G) and CHARMM (H) force fields. The events were identified based on distances between G63 CA atoms in oppositely oriented monomers.

We wondered what might be the reason for the lower stability of the SF in V55E, leading to more frequent inactivation events in simulations. We focused on molecular events happening before the D64 flip, because, as we have shown above, it is an essential feature underlying SF transition to the inactivated state. In the conductive state of the SF, D64 makes hydrogen bonds with Y51 and E55, which adopts the 'vertical' orientation, and there is one water molecule involved in the hydrogen bond network (**Fig. 1 E**). We characterized the time evolution of the orientation of the E55 sidechain ('vertical' vs 'horizontal') and the number of water molecules behind the SF, in simulation before the D64 flip, in both force fields (**Fig. 6 A, B**). As can be seen in these exemplary traces (for all traces see **Supplementary Fig. 13, 14)**, the rotameric transition of the E55 sidechain from 'vertical' to 'horizontal' is accompanied with an additional water molecule entering the space behind the SF. This water molecule can now create a hydrogen bond with the free sidechain of E55 (**Fig. 6 C**) Eventually, more water molecules enter this space, disrupting the hydrogen bond between D64 and Y51, that results in D64 flipping and subsequent dilation of the SF at the level of G63. Interestingly, in these conditions, the 'horizontal' orientation of the E55 sidechain occurs more often in the CHARMM force field as well (**Fig. 6 B**) than in shorter simulations, indicating slower dynamics of this rotameric transition in CHARMM.

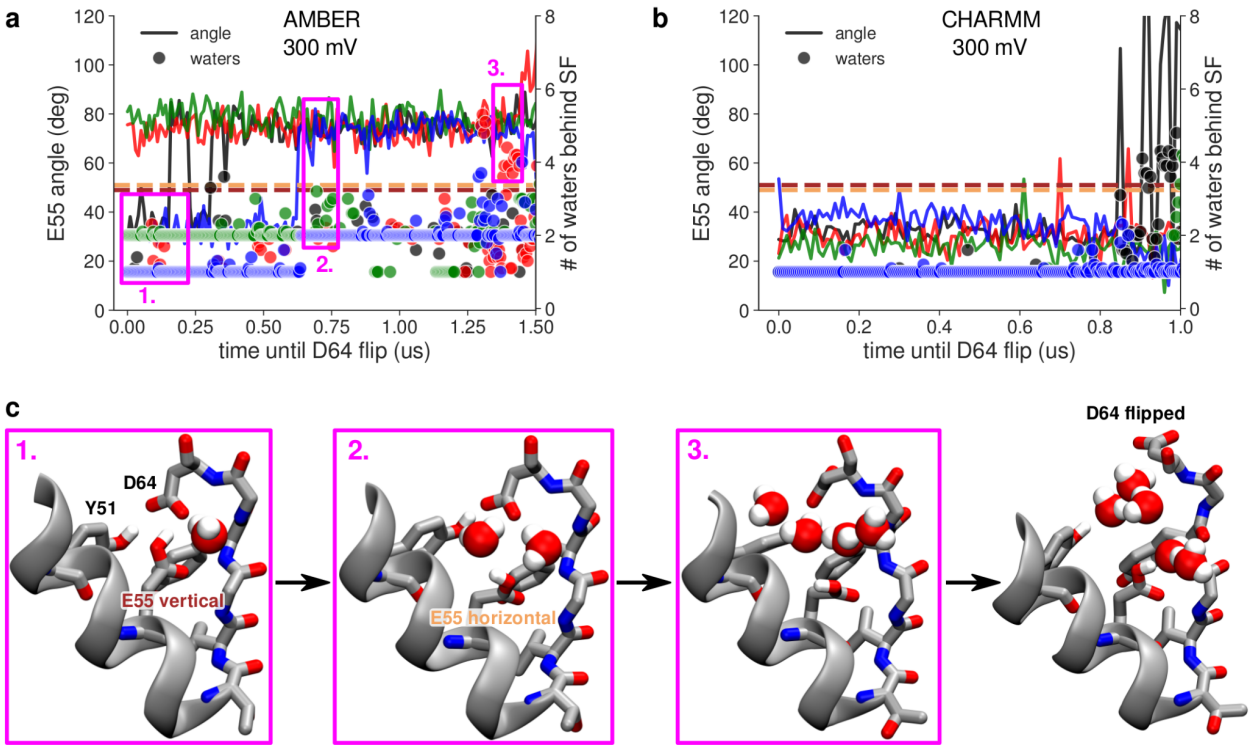

Figure 6 Molecular events leading to D64 flipping and filter inactivation in MD simulations of V55E. A, B Exemplary trajectory traces showing the angle of the E55 side chain (lines) and the number

of water molecules behind the selectivity filter (dots) before the D64 flip. Each color refers to one of the channel monomers. The angle values below 50 degrees (marked as a dashed brown line) indicate the 'vertical' orientation of the E55 sidechain, whereas larger values indicate the 'horizontal' orientation. C, Visualizations of selected timepoints from A (pink boxes) - rotameric transition of the E55 side chain from 'vertical' to 'horizontal' is accompanied with a water flux behind the filter, which eventually leads to the breakage of the D64-Y51 hydrogen bond and D64 flipping.

DISCUSSION

In this work, we set out to better understand the molecular basis for SF gating in MthK WT and the KcsA-like mutant MthK V55E by combining electrophysiological measurements with large scale MD simulations comprising more than 900 us of sampling. Previously, it was established that MthK WT exhibits SF gating at depolarized voltages, similar to C-type inactivation described in KcsA and Kv channels [9,12]. Here, both electrophysiology and computational methods showed that in MthK V55E, the open state of the channel is destabilized. Gating of V55E is characterized by markedly reduced Popen over a wide range of transmembrane voltage (-200 to 200 mV), and at high potassium concentration (200 mM) at both sides of the membrane, as opposed to MthK WT, in which the open state is destabilized depolarized voltages and/or reduced external potassium concentration [9,12].

Two *in silico* electrophysiology simulation-based approaches revealed how the V55E mutation affects ion permeation and SF stability in MthK. In contrast to the KcsA crystal structure, where the side chain of this protonated glutamate exists only in one rotameric state ('vertical orientation'), hydrogen bonding with a conserved aspartate and crystallographically resolved water molecule behind the SF, our MD simulations show that in MthK V55E, the E55 side chain is mobile and can exist in at least two rotameric states, namely 'vertical' and 'horizontal'. The strong interaction between E55 and D64 in the 'vertical' orientation leads to decreased structural plasticity of the SF in its upper part, which increases energetic barriers for ion permeation (in the AMBER force field) and compromises the geometry of the S0 binding site (in the CHARMM force field), resulting in much lower currents through MthK V55E. This strain is relieved when the E55 side chain adopts the 'horizontal' orientation, and then the mutant channel is able to permeate K^+ ions at rates approaching those recorded in MthK WT. Therefore, the ionic current in MthK V55E is regulated not only *via* activation gate - SF coupling (as previously described for MthK WT) [20], but also by the E55 side chain rotameric state. The preference for the 'vertical' vs 'horizontal' orientation also depends on the level of the activation gate opening, revealing a complex activation gate-selectivity filter-pore helix coupling. Despite the differences between the force fields, mostly in predicting the preference of the E55 side chain to adopt the 'horizontal' orientation, we suggest that the reduced Popen of MthK V55E might be partially caused by low permeability of the SF, due to the E55 side chain adopting the 'vertical' orientation. To the best of our knowledge, the 'horizontal' orientation of E55 glutamate (E71 in KcsA) has not been reported before. Further research will address whether both orientations of E71 occur in KcsA as well, or they are exclusive for the MthK channel, due to, for example,

differences in surrounding residues.
Our longer simulations also allowed us to peek into larger conformational transitions of the SF, which may directly relate to the C-type inactivation process. Here, surprisingly, both MthK WT and MthK V55E show behavior more comparable with stably-inactivated Kv channels (*Shaker* W434F and Kv1.2 W362F), rather than with KcsA. Similar asymmetric SF conformations have been also observed in previous simulations of MthK without voltage with a low number of K^+ ions bound to the filter [28], as well as in the structures of some two-pore domain (K2P) potassium channels, TREK-1 [29] and TASK-2 [30]. Specifically, the conformational transitions (inactivation) observed in our MD simulations of both MthK channels occurs *via* widening (dilation) of the SF at the level of 'second' glycines (G63 in MthK), in agreement with available structural data for *Shaker* W434F and Kv1.2 W362F [24,26]. Our simulation data reveal that this dilation follows the breakage of the critical hydrogen bond behind the SF, between D64 and Y55. The strength of this hydrogen bond has been previously directly linked to the rate of inactivation in Kv channels in experiments employing non-natural amino acids [10], further highlighting the converging behavior of MthK and Kv channels with respect to SF gating. When this D64-Y55 hydrogen bond is broken, D64 flips toward the extracellular side ('aspartate flip') allowing the SF to widen. A similar 'aspartate flip' has been recently observed in a combined experimental (x-ray and ssNMR) and computational study on the 'MthK-like' KcsA E71V mutant [31]. In our simulations, the widened SF displays compromised geometries of the ion binding sites, due to outward rotation of carbonyl oxygens ('carbonyl flips') as reported earlier [12,19]. Subsequently, the ion binding sites get filled with water molecules (**Fig 5, D-F**), which disrupts the optimal ion permeation that normally occurs in a water-free fashion *via* direct ion-ion contacts [32]. By directly simulating many inactivation events (20 individual simulations per system/force field), we showed that this process occurs more frequently in MthK V55E than in the WT channel, in both force fields, which is in full agreement with our electrophysiological recordings. Interestingly, our data suggest that the structural basis for reduced stability of the MthK V55E SF is, again, related to the orientation of the E55 side chain. As E55 participates in the intricate hydrogen bond network including D64 and Y55, the rotameric transition of its sidechain from 'vertical' to 'horizontal' leads to a water flux behind the SF, further destabilizing D64-Y55 bond. Indeed, in the 'horizontal' orientation, the hydrophilic side chain of protonated E55 does not have any obvious hydrogen bond partners among protein residues to bond with, thus it attracts additional water molecules from the extracellular side. Interestingly, viral K^+ channels, which also exhibit exquisite SF gating, have similarly hydrophilic Thr or Ser residues in the position equivalent to E55 [33,34], suggesting that a similar molecular behavior might be expected in those channels.

In our simulations, the inactivation process in the MthK channel, arising from SF gating, seems to be structurally related to the same process in Kv channels and less so to the one in KcsA. Thus a single mutation in the pore-helix can simultaneously affect conductive properties and open state stability, leading to inactivation. This is achieved by a functionally relevant rotameric

transition of a hydrophilic residue behind the SF. These results contribute to a conceptual framework for the effects of pore-helix residues on SF gating in various potassium channels.

METHODS

Protein preparation and single-channel recording

MthK was expressed, purified, and reconstituted into proteoliposomes as described previously [35]. Proteoliposomes were composed of *E.coli* lipids (Avanti) and rapidly frozen in liquid N_2 and stored at -80ºC until use. Protein concentrations in proteoliposomes ranged from 5 to 25 µg protein per mg lipid. Mutations were introduced using the QuikChange Site-Directed Mutagenesis Kit (Agilent Technologies) and confirmed by DNA sequencing.

Recordings were obtained using planar lipid bilayers of POPE:POPG (3:1) in a horizontal bilayer chamber, essentially as described previously [12]. For these experiments, solution in the *cis* (top) chamber contained 200 mM KCl, 10 mM HEPES (pH 8.1), 100 µM Cd^{2+}. Solution in the *trans* (bottom) chamber contained either 5 or 200 mM KCl and 10 mM HEPES (pH 7.0). This arrangement ensured that MthK channels incorporated into the bilayer with the cytosolic side facing the *trans* chamber would be silent, whereas channels with the cytosolic side facing the *cis* chamber would be maximally activated (by Cd^{2+}). Within each bilayer, multiple solution changes were performed using a gravity-fed perfusion system that enabled exchange of solution in the *trans* chamber. To ensure completeness of solution changes, the *trans* chamber was washed with a minimum of 10 ml (~10 chamber-volumes) of solution prior to recording under a given set of conditions.

Single-channel currents were amplified using a Dagan PC-ONE patch clamp amplifier with low-pass filtering to give a final effective filtering of 333 Hz (dead time of 0.538 ms), and sampled by computer at a rate of 50 kHz. Currents were analyzed by measuring durations of channel openings and closings at each current level by 50% threshold analysis, using pClamp 9.2. These were used to calculate NPo as:

$$NPo = \sum_{i=1}^{n} iP_i \qquad (1)$$

in which N is the number of channels in the bilayer, i is the open level and P_i is probability of opening at that level. The mean single-channel open probability (Po) is obtained by dividing NPo by N, determined by recording under conditions where the maximum level of channel opening can be observed. The voltage-dependence of Po was described by the Boltzmann equation,

$$Po = Pomax / (1 + \exp(z\delta\,(V-V_{1/2})/k_BT))) \qquad (2)$$

in which *Pomax* is the maximal *Po*, $z\delta$ is the effective gating valence (in e_0), $V_{1/2}$ is the voltage at half-maximal *Po*, k_B is Boltzmann's constant and *T* is temperature. Data points (e.g. *Po* and mean interval durations) are presented as mean ± SEM of three to five observations for each data point, and collectively represent data from a total of 17 different bilayers.

MD simulations

We used the same setup as we used for MthK WT in our recent publication [20], where we thoroughly characterized ion permeation and selectivity filter-activation gate coupling, using the Charmm36m (referred to as CHARMM) [36,37] and Amber14sb (referred to as AMBER) [38] force fields. The data for MthK WT in the current manuscript (black traces) are taken directly from our previous work. For MD simulations of the V55E mutant, the valine residue in MthK WT was replaced by a protonated glutamate from KcsA (PDB ID: 1K4C) after aligning both channels with their (identical) selectivity filters. The resulting structure was further equilibrated for at least 100 ns, whereas all other simulation details and parameters were identical to those used before. After equilibration, we imposed the desired degree of activation gate opening by applying harmonic distance restraints between the CA atoms of the pairs of terminal residues - P19 and F97. The equilibrium distances were adopted from our previous publication, and the resulting average distances are plotted in **Fig. 3 B** and **Fig. 4 A**. The systems were simulated at an external field applied along the z-axis to generate the membrane voltage of ~300 mV. The voltage (*V*) was calculated with:

$$V=EL_z \qquad (3)$$

Where *E* denotes the applied electric field and L_z the length of the simulation box along the z-axis. All simulations were performed with GROMACS MD software, versions 5.1 and 2020 [39–43]. All the simulation settings were identical to our previous work [20]. For each opening and force field, 10 (short simulations) or 20 (long simulations) were performed, each lasting 1 us (short simulations) or 5 us (long simulations), which resulted in a total simulation time (for all systems) of ca. 920 us. Ionic currents were estimated by counting the number of K^+ ions crossing the SF in each simulation, using a custom FORTRAN code (available as a Supplementary Software associated with our previous publication [20]). Remaining quantities were calculated using GROMACS tools - gmx distance (distances), gmx angle (angles) and gmx select (number of water molecules). Most of the presented data (besides individual simulation traces and counts) are averages from at least 10 independent simulation replicas. In all cases, error bars represent 95% confidence intervals. For data analysis, Python 3 was used, together with numpy [44], pandas [45], seaborn, matplotlib [46], scipy [47] and bootstrapped modules. Molecular visualizations were rendered with VMD [48].

Supplemental Material consists of Supplementary Figures 1-14, that show individual traces from 'long' MD trajectories for D64 - Y51 distances (Supplementary Figures 1-4), for G61 CA-CA

distances (Supplementary Figures 5-8), for G63 CA-CA distances (Supplementary Figures 9-12) and for E55 angle and number of water molecules behind the SF (Supplementary Figures 13-14).

ACKNOWLEDGEMENTS

We thank Simon Bernèche and Florian Heer for many important insights. This research was supported by the German Research Foundation (DFG) through FOR2518 'Dynion', Project P5 (W.K. and B. L. dG.) and National Institutes of Health grant R01 GM126581 (B.S.R.).

AUTHOR CONTRIBUTIONS

B.S.R., W.K. and B. L. dG. conceived the project. A.S.T. performed and analyzed the electrophysiological recordings. W.K. performed and analyzed MD simulations. W.K. B.S.R. and B. L. dG. wrote the manuscript.

REFERENCES

[1] B. Hille, Ion Channels of Excitable Membranes, Third Edition, (n.d.) 11.

[2] G. Panyi, C. Deutsch, Cross Talk between Activation and Slow Inactivation Gates of *Shaker* Potassium Channels, J. Gen. Physiol. 128 (2006) 547–559. https://doi.org/10.1085/jgp.200609644.

[3] G. Yellen, The moving parts of voltage-gated ion channels, Q. Rev. Biophys. 31 (1998) 239–295. https://doi.org/10.1017/S0033583598003448.

[4] M.O. Jensen, V. Jogini, D.W. Borhani, A.E. Leffler, R.O. Dror, D.E. Shaw, Mechanism of Voltage Gating in Potassium Channels, Science. 336 (2012) 229–233. https://doi.org/10.1126/science.1216533.

[5] G. Yellen, The voltage-gated potassium channels and their relatives, Nature. 419 (2002) 35–42. https://doi.org/10.1038/nature00978.

[6] J.F. Cordero-Morales, L.G. Cuello, Y. Zhao, V. Jogini, D.M. Cortes, B. Roux, E. Perozo, Molecular determinants of gating at the potassium-channel selectivity filter, Nat. Struct. Mol. Biol. 13 (2006) 311–318. https://doi.org/10.1038/nsmb1069.

[7] J.F. Cordero-Morales, V. Jogini, A. Lewis, V. Vásquez, D.M. Cortes, B. Roux, E. Perozo, Molecular driving forces determining potassium channel slow inactivation, Nat. Struct. Mol. Biol. 14 (2007) 1062–1069. https://doi.org/10.1038/nsmb1309.

[8] Y. Xu, A.E. McDermott, Inactivation in the potassium channel KcsA, J. Struct. Biol. X. 3 (2019) 100009. https://doi.org/10.1016/j.yjsbx.2019.100009.

[9] A.S. Thomson, B.S. Rothberg, Voltage-dependent inactivation gating at the selectivity filter of the MthK K+ channel, J. Gen. Physiol. 136 (2010) 569–579. https://doi.org/10.1085/jgp.201010507.

[10] S.A. Pless, J.D. Galpin, A.P. Niciforovic, H.T. Kurata, C.A. Ahern, Hydrogen bonds as molecular timers for slow inactivation in voltage-gated potassium channels, ELife. 2 (2013) e01289. https://doi.org/10.7554/eLife.01289.

[11] R. Schönherr, S.H. Heinemann, Molecular determinants for activation and inactivation of HERG, a human inward rectifier potassium channel., J. Physiol. 493 (1996) 635–642. https://doi.org/10.1113/jphysiol.1996.sp021410.

[12] A.S. Thomson, F.T. Heer, F.J. Smith, E. Hendron, S. Bernèche, B.S. Rothberg, Initial steps of inactivation at the K^+ channel selectivity filter, Proc. Natl. Acad. Sci. 111 (2014). https://doi.org/10.1073/pnas.1317573111.

[13] J. López-Barneo, T. Hoshi, S.H. Heinemann, R.W. Aldrich, Effects of external cations and mutations in the pore region on C-type inactivation of Shaker potassium channels,

Receptors Channels. 1 (1993) 61–71.
[14] T. Baukrowitz, G. Yellen, Modulation of K+ current by frequency and external [K+]: a tale of two inactivation mechanisms, Neuron. 15 (1995) 951–960. https://doi.org/10.1016/0896-6273(95)90185-x.
[15] T. Baukrowitz, G. Yellen, Use-dependent blockers and exit rate of the last ion from the multi-ion pore of a K+ channel, Science. 271 (1996) 653–656. https://doi.org/10.1126/science.271.5249.653.
[16] T. Baukrowitz, G. Yellen, Two functionally distinct subsites for the binding of internal blockers to the pore of voltage-activated K^+ channels, Proc. Natl. Acad. Sci. 93 (1996) 13357–13361. https://doi.org/10.1073/pnas.93.23.13357.
[17] A. Suma, D. Granata, A.S. Thomson, V. Carnevale, B.S. Rothberg, Polyamine blockade and binding energetics in the MthK potassium channel, J. Gen. Physiol. 152 (2020) e201912527. https://doi.org/10.1085/jgp.201912527.
[18] F.J. Smith, V.P.T. Pau, G. Cingolani, B.S. Rothberg, Structural basis of allosteric interactions among Ca2+-binding sites in a K+ channel RCK domain, Nat. Commun. 4 (2013) 2621. https://doi.org/10.1038/ncomms3621.
[19] J.T. Brennecke, B.L. de Groot, Mechanism of Mechanosensitive Gating of the TREK-2 Potassium Channel, Biophys. J. 114 (2018) 1336–1343. https://doi.org/10.1016/j.bpj.2018.01.030.
[20] W. Kopec, B.S. Rothberg, B.L. de Groot, Molecular mechanism of a potassium channel gating through activation gate-selectivity filter coupling, Nat. Commun. 10 (2019) 5366. https://doi.org/10.1038/s41467-019-13227-w.
[21] L.G. Cuello, V. Jogini, D.M. Cortes, E. Perozo, Structural mechanism of C-type inactivation in K+ channels, Nature. 466 (2010) 203–208. https://doi.org/10.1038/nature09153.
[22] J. Li, J. Ostmeyer, L.G. Cuello, E. Perozo, B. Roux, Rapid constriction of the selectivity filter underlies C-type inactivation in the KcsA potassium channel, J. Gen. Physiol. (2018) jgp.201812082. https://doi.org/10.1085/jgp.201812082.
[23] J. Li, R. Shen, A. Rohaim, R. Mendoza Uriarte, M. Fajer, E. Perozo, B. Roux, Computational study of non-conductive selectivity filter conformations and C-type inactivation in a voltage-dependent potassium channel, J. Gen. Physiol. 153 (2021) e202112875. https://doi.org/10.1085/jgp.202112875.
[24] R. Reddi, K. Matulef, E.A. Riederer, M.R. Whorton, F.I. Valiyaveetil, Structural basis for C-type inactivation in a Shaker family voltage gated K^+ channel, Biochemistry, 2021. https://doi.org/10.1101/2021.10.01.462615.
[25] Y. Zhou, Chemistry of ion coordination and hydration revealed by a K+ channel±Fab complex at 2.0 AÊ resolution, 414 (2001) 6.
[26] X.-F. Tan, C. Bae, R. Stix, A.I. Fernández-Mariño, K. Huffer, T.-H. Chang, J. Jiang, J.D. Faraldo-Gómez, K.J. Swartz, Structure of the Shaker Kv channel and mechanism of slow C-type inactivation, Sci. Adv. 8 (2022) eabm7814. https://doi.org/10.1126/sciadv.abm7814.
[27] W. Kopec, D.A. Köpfer, O.N. Vickery, A.S. Bondarenko, T.L.C. Jansen, B.L. de Groot, U. Zachariae, Direct knock-on of desolvated ions governs strict ion selectivity in K+ channels, Nat. Chem. 10 (2018) 813–820. https://doi.org/10.1038/s41557-018-0105-9.
[28] Boiteux Céline, Posson David J., Allen Toby W., Nimigean Crina M., Selectivity filter ion binding affinity determines inactivation in a potassium channel, Proc. Natl. Acad. Sci. 117 (2020) 29968–29978. https://doi.org/10.1073/pnas.2009624117.
[29] M. Lolicato, A.M. Natale, F. Abderemane-Ali, D. Crottès, S. Capponi, R. Duman, A. Wagner, J.M. Rosenberg, M. Grabe, D.L. Minor, K_{2P} channel C-type gating involves asymmetric selectivity filter order-disorder transitions, Sci. Adv. 6 (2020) eabc9174. https://doi.org/10.1126/sciadv.abc9174.
[30] B. Li, R.A. Rietmeijer, S.G. Brohawn, Structural basis for pH gating of the two-pore domain K+ channel TASK2, Nature. 586 (2020) 457–462.

https://doi.org/10.1038/s41586-020-2770-2.
[31] A. Rohaim, B.J.A. Vermeulen, J. Li, F. Kümmerer, F. Napoli, L. Blachowicz, J. Medeiros-Silva, B. Roux, M. Weingarth, A different mechanism of C-type inactivation in the Kv-like KcsA mutant E71V, Molecular Biology, 2021. https://doi.org/10.1101/2021.09.22.461404.
[32] A. Mironenko, U. Zachariae, B.L. de Groot, W. Kopec, The Persistent Question of Potassium Channel Permeation Mechanisms, J. Mol. Biol. 433 (2021) 167002. https://doi.org/10.1016/j.jmb.2021.167002.
[33] C.J. Braun, C. Lachnit, P. Becker, L.M. Henkes, C. Arrigoni, S.M. Kast, A. Moroni, G. Thiel, I. Schroeder, Viral potassium channels as a robust model system for studies of membrane–protein interaction, Biochim. Biophys. Acta BBA - Biomembr. 1838 (2014) 1096–1103. https://doi.org/10.1016/j.bbamem.2013.06.010.
[34] A.E.V. Andersson, M.A. Kasimova, L. Delemotte, Exploring the Viral Channel KcvPBCV-1 Function via Computation, J. Membr. Biol. 251 (2018) 419–430. https://doi.org/10.1007/s00232-018-0022-2.
[35] V.P.T. Pau, K. Abarca-Heidemann, B.S. Rothberg, Allosteric mechanism of Ca^{2+} activation and H^{+}-inhibited gating of the MthK K^{+} channel, J. Gen. Physiol. 135 (2010) 509–526. https://doi.org/10.1085/jgp.200910387.
[36] A.D. MacKerell, D. Bashford, M. Bellott, R.L. Dunbrack, J.D. Evanseck, M.J. Field, S. Fischer, J. Gao, H. Guo, S. Ha, D. Joseph-McCarthy, L. Kuchnir, K. Kuczera, F.T. Lau, C. Mattos, S. Michnick, T. Ngo, D.T. Nguyen, B. Prodhom, W.E. Reiher, B. Roux, M. Schlenkrich, J.C. Smith, R. Stote, J. Straub, M. Watanabe, J. Wiórkiewicz-Kuczera, D. Yin, M. Karplus, All-atom empirical potential for molecular modeling and dynamics studies of proteins, J. Phys. Chem. B. 102 (1998) 3586–3616. https://doi.org/10.1021/jp973084f.
[37] J. Huang, S. Rauscher, G. Nawrocki, T. Ran, M. Feig, B.L. de Groot, H. Grubmüller, A.D. MacKerell, CHARMM36m: an improved force field for folded and intrinsically disordered proteins, Nat. Methods. 14 (2017) 71–73. https://doi.org/10.1038/nmeth.4067.
[38] J.A. Maier, C. Martinez, K. Kasavajhala, L. Wickstrom, K.E. Hauser, C. Simmerling, ff14SB: Improving the Accuracy of Protein Side Chain and Backbone Parameters from ff99SB, J. Chem. Theory Comput. 11 (2015) 3696–3713. https://doi.org/10.1021/acs.jctc.5b00255.
[39] H.J.C. Berendsen, D. van der Spoel, R. van Drunen, GROMACS: A message-passing parallel molecular dynamics implementation, Comput. Phys. Commun. 91 (1995) 43–56. https://doi.org/10.1016/0010-4655(95)00042-E.
[40] B. Hess, C. Kutzner, D. van der Spoel, E. Lindahl, GROMACS 4: Algorithms for Highly Efficient, Load-Balanced, and Scalable Molecular Simulation, J. Chem. Theory Comput. 4 (2008) 435–447. https://doi.org/10.1021/ct700301q.
[41] M.J. Abraham, T. Murtola, R. Schulz, S. Páll, J.C. Smith, B. Hess, E. Lindahl, GROMACS: High performance molecular simulations through multi-level parallelism from laptops to supercomputers, SoftwareX. 1–2 (2015) 19–25. https://doi.org/10.1016/j.softx.2015.06.001.
[42] E. Lindahl, B. Hess, D. van der Spoel, GROMACS 3.0: a package for molecular simulation and trajectory analysis, Mol. Model. Annu. 7 (2001) 306–317. https://doi.org/10.1007/s008940100045.
[43] S. Pronk, S. Páll, R. Schulz, P. Larsson, P. Bjelkmar, R. Apostolov, M.R. Shirts, J.C. Smith, P.M. Kasson, D. van der Spoel, B. Hess, E. Lindahl, GROMACS 4.5: a high-throughput and highly parallel open source molecular simulation toolkit, Bioinformatics. 29 (2013) 845–854. https://doi.org/10.1093/bioinformatics/btt055.
[44] T.E. Oliphant, Python for Scientific Computing, Comput. Sci. Eng. 9 (2007) 10–20. https://doi.org/10.1109/MCSE.2007.58.
[45] W. McKinney, pandas: a Foundational Python Library for Data Analysis and Statistics, (n.d.) 10.

[46] J.D. Hunter, Matplotlib: A 2D Graphics Environment, Comput. Sci. Eng. 9 (2007) 90–95. https://doi.org/10.1109/MCSE.2007.55.
[47] E. Jones, T. Oliphant, P. Peterson, others, SciPy: Open source scientific tools for Python, 2001. http://www.scipy.org/.
[48] W. Humphrey, A. Dalke, K. Schulten, VMD: Visual molecular dynamics, J. Mol. Graph. 14 (1996) 33–38. https://doi.org/10.1016/0263-7855(96)00018-5.